




Electrical transport mechanisms of Neodymium-doped rare-earth semiconductors

Isabela C. F. Vaz¹, Carlos Eugenio Macchi², Alberto Somoza², Leandro S. R. Rocha³, Elson Longo^{3,*} , Luis Cabral⁴, Edison Z. da Silva⁴, Alexandre Zirpoli Simões⁵, Giulia Zonta⁶, Cesare Malagù⁶, P. Mariela Desimone⁷, Miguel Adolfo Ponce⁷, and Francisco Moura¹

¹Advanced Materials Interdisciplinary Laboratory, Federal University of Itajubá, Unifei Campus Itabira, Itabira, MG, Brazil

²Institute of Materials Physics of Tandil-IFIMAT (UNCPBA) and UE CIFICEN (UNCPBA-CICPBA-CONICET), Tandil, Argentina

³Center for Research and Development of Functional Materials (CDMF), Federal University of São Carlos - (UFSCar), São Carlos, SP, Brazil

⁴Institute of Physics "Gleb Wataghin" (IFGW), State University of Campinas, Campinas, SP, Brazil

⁵São Paulo State University (UNESP), School of Engineering, Guaratinguetá, SP, Brazil

⁶Department of Physics and Earth Sciences, University of Ferrara, Via Savonarola, Ferrara, Italy

⁷Institute of Materials Science and Technology (INTEMA), National University of Mar del Plata, Mar del Plata, Argentina

Received: 23 December 2021

Accepted: 14 March 2022

© The Author(s), under exclusive licence to Springer Science+Business Media, LLC, part of Springer Nature 2022

ABSTRACT

This study reports the electrical properties of Nd-doped cerium oxide (CeO₂) films synthesized by microwave assisted hydrothermal using a two-point probe technique. Positron annihilation lifetime spectroscopy studies evidenced that, as the Nd content rises, a structural disorder occurs. This is caused by an increase in oxygen vacancies surrounded with Nd (defective clusters), with the mean lifetime components ranging between 290 and 300 ps. Particle size estimation showed values from 8.6 to 28.9 nm. Along with the increase of neodymium impurities, also the conductivity increases, due to the hopping conduction mechanism between defective species. This gives rise to a response time of only 6 s, turning these materials candidates to realize gas sensor devices. Ab initio investigations showed that the improved electric conduction is boosted mostly by the reduced Nd²⁺ than the Ce³⁺, where the oxygen vacancies play a fundamental role.

1 Introduction

CeO₂ is a n-type multifunctional semiconductor material, featuring numerous applications, such as catalysis or active support for catalysis,

photocatalysis, biomedical applications (due to its low toxicity), and can also be employed as a gas adsorbent and in sensors realization [1–5].

Traditionally, CeO₂ crystals are prepared by coprecipitation [6], polymeric precursor [7], and conventional hydrothermal methods [8–11]. On the other

Address correspondence to E-mail: elson.liec@gmail.com

hand, the Microwave-Assisted Hydrothermal (MAH) route is a convenient, fast, and cost-effective method, which uses microwaves during the hydrothermal synthesis to increase the conventional crystallization kinetics by one to two orders of magnitude. The same principle used in MAH is also applied in the microwave-assisted solvothermal (MAS) route; however, the later employs a non-aqueous solvent (e.g., alcohols and glycols). Concerning the synthesis conditions for CeO₂ nanocrystals, our group optimized the parameters for nanoparticles preparation, using the MAH method for pure and (RE)-doped CeO₂, leading to agglomerated nanostructured particles at 100 °C for 8 min [12, 13], using 2 M KOH as the mineralizer agent.

Besides, the doping of ceria nanocrystals with rare-earth elements such as praseodymium, gadolinium, lanthanum, and neodymium creates oxygen vacancies, thereby enabling the migration of oxygen ions through the lattice [14, 15]. As a result, the modified materials can have chemical and physical properties that differ from their pure counterparts [16].

Valuable information about changes in the structural defects at nanoscale due to the doping level in ceria can be obtained using the nuclear technique Positron Annihilation Lifetime Spectroscopy (PALS) [17]. Positrons have a particular tendency to be trapped by vacancy-like defects in solids. PALS is considered the most sensitive experimental technique to study vacancy-like defects, given that it simultaneously provides information on quantity and selectivity of this defect type in solids, particularly in semiconductors [18].

Considering the detection of gases using nanostructured materials, for a n-type semiconductor, the sensing mechanism can be explained through the reactions occurring on its surface, when in contact with gaseous analyte or vapor. Since these materials are exposed to air, O₂ is adsorbed on the surface, capturing electrons from the metal-oxide surface (MOxS), and creating oxygen anionic species (O₂⁻, O⁻, O²⁻) that cause the formation of a surface depletion layer. Once the sensor comes in contact with a reducing gas/vapor, such molecules are adsorbed on the MOxS, reacting with the oxygen species, which are removed from the surface and electrons are released back to the MOxS. This behavior results in the decay of the sensor resistance that consists in its signal/response. Usually, the sensing mechanism of a n-type MOxS of the n-type

for detection of a reducing atmosphere at high temperatures, leads to the generation of oxygen vacancies and the reduction of Ce(IV) to Ce(III) [19].

Several studies reported the synthesis and fabrication of gas sensing devices to detect volatile organic compounds (VOC) [20], including ethanol and methanol [21], acetone [22], besides hydrogen detection [23, 24]. Additionally, despite the more than 9.000 results found on the Springer Link database on “carbon monoxide and gas sensor”, the several cases of unintentional carbon monoxide (CO) intoxication continues to grow worldwide, in parallel with the socio-demographic index (SDI) [25]. This means that more attention must be given in the CO detection and monitoring, which has been named “the unnoticed poison of the twenty-first century”.

The CeO₂ properties at atomistic level have been reported using density functional theory (DFT) calculations. The generalized gradient approximation is an efficient tool to investigate the electronic properties of the ceria dioxide, where the Hubbard U correction on 4f-Ce states has been used to improve the understanding of the electronic band structure of this material [26]. Our group has devoted significant efforts in developing CeO₂ films for CO gas sensing, previously demonstrating that the electrical measurements in different gas atmospheres lead to an n-type semiconducting behavior for Pr-doped CeO₂. PALS revealed that the concentration of the vacancy-like group defects of the samples depends on the atmosphere under which the thermal treatment was performed. Here vacancies played a major role in the Ce³⁺ formation, thereby increasing the available 4f¹ electrons for the consequent cluster-to-cluster charge transfer (CCCT) process. Moreover, we developed a semiconductor nanomaterial that can produce white light, showing to be promising as a single-material white-light-emitting source. Furthermore, we showed that its structures and light-emitting properties can be systematically tuned [27].

In the present investigation, and as a natural extension of previous works, pure and Nd-doped CeO₂ nanomaterials were synthesized through the MAH process to analyze the structural properties and the electrical behavior of thick films under air and CO atmospheres. We expect the incorporation of Nd ions into the ceria lattice to substitute surface cerium ions, resulting in a higher concentration of oxygen vacancy (V_o) defective species when compared to the La [28, 29] and Pr-doped [27] systems.

As the amount of oxygen vacancies varies depending on surface morphology (which influences lattice defects and oxygen mobility), the Fermi level (E_F) and the 4f state position change due to gas absorption on the surface. This changes the number of available conduction electrons (4f state electrons $4f^0 \rightarrow 4f^1$ when Ce^{4+} reduces to Ce^{3+}) affecting the recovery and response times.

A proposed mechanism caused by defective species shows that an increase of the Nd content in the cerium dioxide samples favored the formation of a higher concentration of small neutral $Nd^{2+}-V_O$ species, making these materials great candidates for gas sensor devices. Measurements of conductivity as a function of temperature were conducted to determine the film sensitivity under different atmospheres as well as to correlate this parameter with the defect structure. Furthermore, the interplay with theoretical calculations was performed using DFT investigations, to understand the localized magnetic moments in defective geometries. This allowed us to study the reduction of Ce and Nd atoms, where the calculated formation energies indicate the most stable thermodynamic defect in the growth phase.

2 Experimental procedure and calculation details

2.1 Synthesis of pure and doped rare-earth elements

$Ce_{1-(3/4)x}Nd_xO_2$ ($x = 0.00; 0.04; 0.08$ and $x = 0.12$) nanopowders were synthesized via MAH method, according to the procedures described in literature [30], using a precursor solution of Cerium (III) nitrate hexahydrate ($Ce(NO_3)_3 \cdot 6H_2O$, 99%, Sigma-Aldrich). The Nd atoms were obtained by dissolving Neodymium dioxide (Nd_2O_3 , 99%, Sigma-Aldrich) under constant stirring and heating (60 °C) assisted by Nitric Acid (HNO_3 , 65%, Labsynth). The synthesized $Ce_{1-(3/4)x}Nd_xO_2$ powders (with 0, 4, 8, and 12% Nd doping) were labeled as P0, P4, P8, and P12, respectively.

2.2 Structural characterization of the pure and doped rare-earth elements

The crystals were structurally characterized by X-ray diffraction (XRD), using a D/Max-2000PC Rigaku

(Japan) diffractometer with Cu $K\alpha$ radiation ($\lambda = 1.5406 \text{ \AA}$) in the 2θ range from 20 to 110°, with a scanning velocity of 0.2°/min in the Rietveld routine [31] and the graphical user interface EXPGUI developed by Toby [32]. Raman spectroscopy and UV-Vis spectroscopy analyses were recorded at the same conditions, according to a previous research article [30]. To determine the optical band gap energy, the plot of $(h\nu\alpha)^2$ as a function of $h\nu$ is known as the Tauc plot [33].

Positron Lifetime spectra were acquired using a *Positron Lifetime Picosecond Timing System ORTEC*® in a co-linear geometry with a time resolution of 210 ps. 10 μCi of $^{22}\text{NaCl}$ (radionuclides Product Number: NEZ081 produced by Perkin-Elmer) deposited onto two thin Kapton foils was used as positron source. PALS spectra of $\sim 2 \times 10^6$ counts were collected at room temperature and then analyzed using the LT10 code [34].

2.3 Film conformation and electrical characterization

The film preparation of the pure (F0) and 4% (F4), 8% (F8), and 12% (F12)-doped samples and their surface characterization were done, using the same conditions previously described [27]. The electrical measurements were carried out with an optoelectronic device (Patents INPI Argentina 201501039539 and INPI Brazil 10 2016 028383 3) [35, 36]. The optoelectronic characterization chamber is a closed chamber in which three heating and cooling cycles up to 420 °C were performed before measuring the resistance values, to eliminate the humidity. Electrical response measurements were carried out as a function of temperature in vacuum, air, and CO atmospheres at a constant pressure of 100 mmHg. After determining the operation temperature, the electrical resistance of the films was measured as a function of time. An excitation current of 1 mA was applied by using a two-point probe technique with a DC-type measurement. An Agilent 3440A multimeter was employed for the electrical conductance measurements.

2.4 Theoretical approach and computational details

To study the electronic properties of neodymium-doped ceria dioxide, calculations at an atomistic level

based on density functional theory (DFT) investigations [37–39] were performed within the spin-polarized generalized gradient approximation (GGA). The Perdew–Burke–Ernzerhof (PBE) [40] exchange and correlation energy functional were employed, which provides a suitable description of the electronic band structure for ceria dioxide systems [41]. The Kohn–Sham equation was solved using the projector augmented wave (PAW) method [42, 43], where the valence states used in the calculations for cerium, oxygen, and neodymium atoms were $4f^15d^16s^2$, $2s^22p^4$, and $4f^46s^2$, respectively, as implemented in the Vienna ab initio simulation package (VASP) [44–46], version 5.4.4. The equilibrium bulk volume was reached by performing stress tensor minimization, with a plane wave extension of 829 eV, while for the atomic force optimizations, a cutoff of 466 eV was applied (which is 12.5% larger than the value recommended by the VASP package). The slow (fast) convergence for the stress tensor (atomic forces) is due to the number of plane waves used in the calculation. For the Brillouin-zone integration, a $2 \times 2 \times 2$ k-mesh for the stress tensor and atomic force optimizations were employed, and twice of this value for the electronic properties. To avoid partial occupation in the description of electronic states, a Gaussian smearing of 0.01 eV was used in all calculations. The adopted self-consistent convergence criteria were 10^{-6} eV, and the atoms were allowed to move until all the forces were smaller than 0.01 eV/Å on each atom. An improved description for electronic band structure was obtained by using the on-site Hubbard correction (PBE + U) methodology, as proposed by Dudarev et al. [47], where Hubbard U corrections were 4.50 eV, 5.0 eV, and 5.50 eV on 4f-Nd, 4f-Ce, and p-O states, respectively, in agreement with Refs. [19, 26, 48].

3 Results and discussion

3.1 Characterization of nanoparticles

Figure 1 illustrates the structural refinement plot for $\text{Ce}_{1-(3/4)x}\text{Nd}_x\text{O}_2$ nanoparticles with different compositions. The powders are polycrystalline in nature with a cubic fluorite structure and a space group Fm3m is clear, with all diffraction peaks in agreement with the Inorganic Crystal Structure Database (ICSD) card no 72155 [49]. No secondary phase was detected,

suggesting that Nd^{3+} ions were substitutionally incorporated into the CeO_2 lattice, causing the peaks to shift to lower angles owing to the greater ionic radius of Nd^{3+} relative to Ce^{4+} ions, indicating the existence of a solid solution [50]. This change in the electron density of atoms is correlated to the spin–orbit interaction and the formation of polarons. The Rietveld refinement indicated the agreement between observed XRD patterns and theoretical results, with its parameters reported in Table 1. The small variations observed among the values can be related to the peculiarity of each doping percentage, in which distinct Nd content could influence the organization of the octahedral $[\text{CeO}_8]$ and $[\text{NdO}_8]$ clusters within the cubic fluorite structure. Furthermore, it likely caused the formation or the modification of structural defects (i.e., oxygen vacancies, distortion on the bonds, stresses, and strains on the crystalline lattice). Along with the increase in the Nd concentration, there was an increase in the lattice parameter and, consequently, of the unit cell volume, owing to the formation of a solid solution in the CeO_2 crystal lattice. Here the presence of the Nd atom likely increased the London dispersion forces and created different electronic densities by modifying defects at long range. This resulted in a slight increase in the distance between the atoms, influencing lattice parameters, also identified by Nurhasanah [51].

The small variations observed among the values can be related to the peculiarity of each doping percentage, in which distinct Nd electron density could influence the organization of the octahedral $[\text{CeO}_8]$ and $[\text{NdO}_8]$ clusters within the cubic fluorite structure, causing electronic nanostress on the structure (Supplementary Material).

Figure 2 shows the Raman spectrum of both pure and doped CeO_2 with 4, 8, and 12% of Nd, respectively. The peak at 461 cm^{-1} in the CeO_2 pure spectra was related to the cubic fluorite structure–metal dioxide [13]. This result was consistent with those obtained through XRD. A comparison of the spectra with different Nd concentrations showed that the most intense peak at 461 cm^{-1} , due to Ce–O Raman vibrations, shifted toward lower frequencies. As the short-distance induction interaction caused polarization in neighboring clusters, the ceria clusters had lower electron density than the Nd clusters. By contrast, neodymium clusters generated a nanostress in the crystal structure due to the variation of the electronic density of the clusters and the formation of

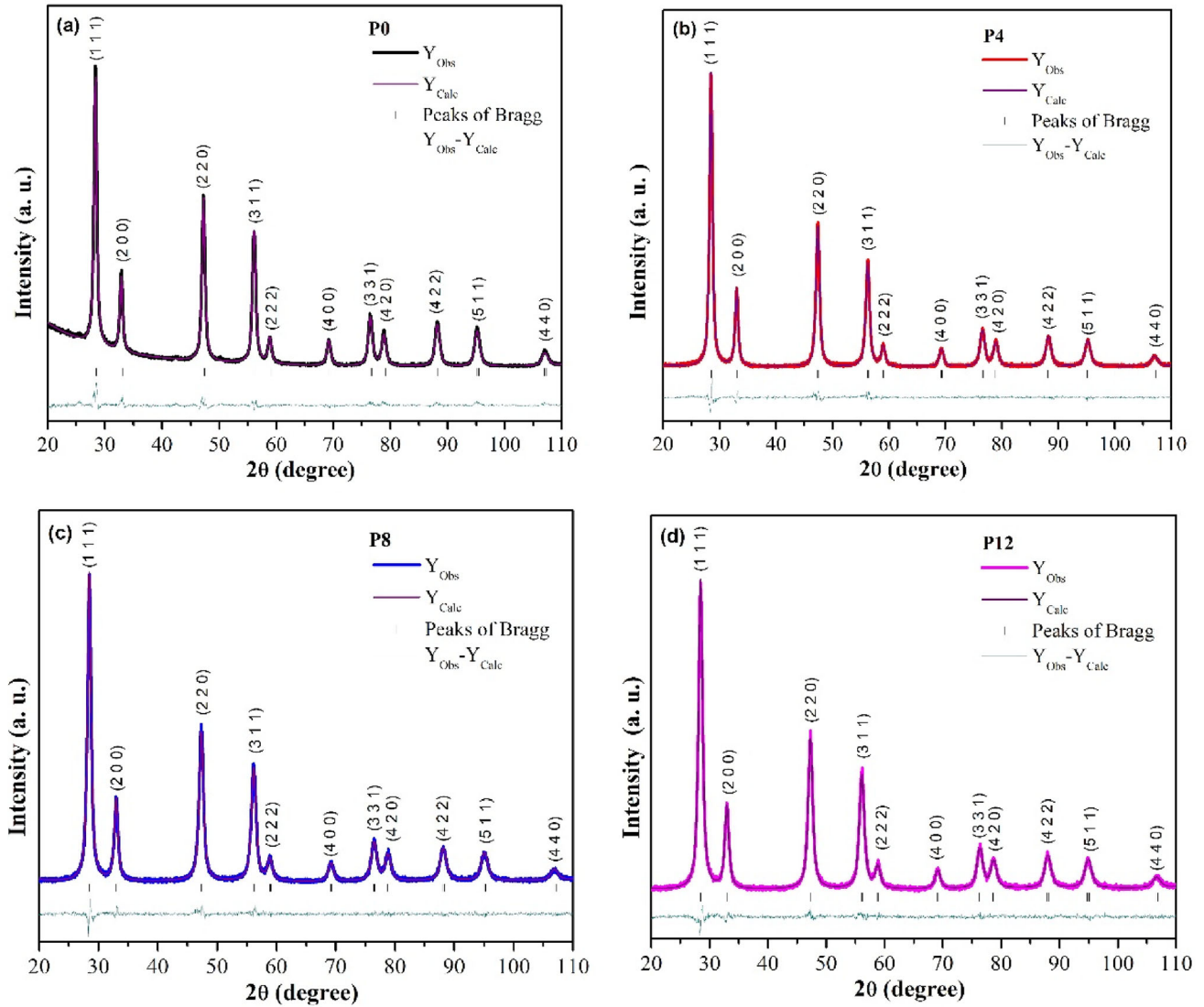


Fig. 1 Rietveld refinement for different Nd contents: **a** P0; **b** P4; **c** P8; and **d** P12

Table 1 Rietveld refinement data for the pure and neodymium-doped nanoparticles

Samples	Lattice parameters $a = b = c$ (Å)	Unit cell volume (Å ³)	R_{Bragg} (%)	R_{wp} (%)	R_p (%)	χ^2
P0	5.4175	159.001	4.70	5.29	4.23	1.49
P4	5.4220	159.404	1.31	5.10	4.07	1.50
P8	5.4285	159.972	1.76	4.89	3.88	1.29
P12	5.4351	160.553	1.64	4.86	3.84	1.31

oxygen vacancies, which enhanced the n-type semi-conducting behavior. Note also that the introduction of a heavier species in the lattice led to an expansion of the crystal lattice parameters, in turn leading to a mode of the Ce–O Raman vibrations shifted toward

lower frequencies. Given that an Nd³⁺ ion has an electronic density markedly larger than a Ce⁴⁺ ion, clusters formed by Nd are bulkier and have different vibrational modes than Ce clusters in the crystal structure. It is important to point out that the results

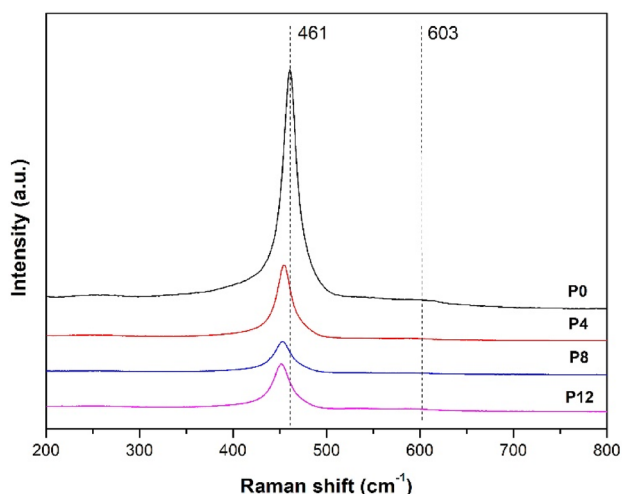


Fig. 2 Raman spectrum of cerium nanoparticles with different Nd contents: P0; P4; P8; and P12

obtained through Raman spectroscopy and XRD were consistent. A weaker Raman band was also observed at 593–606 cm^{-1} , owing to the defect-induced mode at the spectra of both pure and neodymium-doped CeO_2 films. These defects could be the influence of the electron density of Nd clusters, associated with oxygen vacancies in the CeO_2 lattice.

It is possible to calculate the average size of the CeO_2 clusters by the following equation [51]:

$$\Gamma - 10 \text{ cm}^{-1} = 124.7/d \quad (1)$$

where Γ , expressed in cm^{-1} , is half the width of the Raman peak of the Ce–O Raman vibration and d is the average size in nm. The calculation of d by (1) shows that the size of CeO_2 clusters for pure powder is 8.6 nm. The particle sizes were 28.9 nm, 15.6 nm, and 18.6 nm for 4%, 8%, and 12% of Nd, respectively.

Worth mentioning that other methods can also be used to describe the average particle sizes, as the Williamson–Hall equation, used by S.K., Abdel-Aal et al. [52] to determine the influence of graphene on the structure of rare-earth perovskites, besides the four different theoretical approaches used to calculate the particle sizes of CuO-graphene nanocomposites, with values ranging between 20 and 60 nm, in accordance with SEM observations [53].

The relative intensity ratio of I_{606}/I_{461} followed the sequence $P0 < P4 < P8 < P12$, indicating that the P12 sample had the most intrinsic defect sites, while P0 had the least intrinsic ones. Figure 1 also shows a decrease in the intensity of the Raman peaks as the concentration of Nd increased. These results indicate

that the presence of Nd influenced the short-range order crystallinity of the material.

3.2 Influence of Nd doping on structural vacancy-like defects

For all the samples studied, PALS spectra were satisfactorily decomposed considering three discrete lifetime components, after subtracting the background and the source contribution. Each component, corresponding to the formation probability of a particular positron state i , was characterized by a positron lifetime τ_i and by its associated intensity I_i . Such state can be delocalized in the crystal lattice, being so a “bulk state” (τ_b); or localized at a positron trap, i.e., a vacancy-like defect site τ_d , where τ_d is higher than τ_b . The difference between these two lifetimes (τ_b and τ_d) strongly increases with the growth of the open volume associated with a positron trap [18]. Additionally, it is well known that in PALS spectra, the positron mean lifetime $\tau_m = \sum_i I_i \tau_i$ is considered the most robust statistical parameter [18].

In all the measured spectra, a long-lived lifetime of about 1500–2000 ps with an associated intensity $I_3 < 1\%$ was found. According to the literature, such a long-lived lifetime component can be ascribed to the ortho-positronium annihilation via the pick-off process. Considering the small value of I_3 , and following the procedure already reported in the literature [54, 55], from this point on, this lifetime component will be not considered for the interpretation and discussion of our PALS results.

In Fig. 3, we present the evolution of the characteristic positron lifetime parameters obtained from the decomposition of PALS spectra measured for the synthesized $\text{Ce}_{1-3/4x}\text{Nd}_x\text{O}_2$ samples as a function of the Nd content ($x = 0.00; 0.04; 0.08; \text{ and } 0.12$). The first panel in Fig. 3a shows that, the increase of the positron mean lifetime when Nd was added to CeO_2 , indicated that this addition induced the formation of more open volume defects with respect to pure ceria samples. Besides, the constancy within the error bars of τ , obtained by measuring the samples doped with 4 and 8% of Nd, indicates that, for intermediate doping levels, the defect concentration remains the same. Furthermore, for the samples with the highest Nd content, the significant increase of the positron mean lifetime points out a significant increase of the open volumes acting as positron traps.

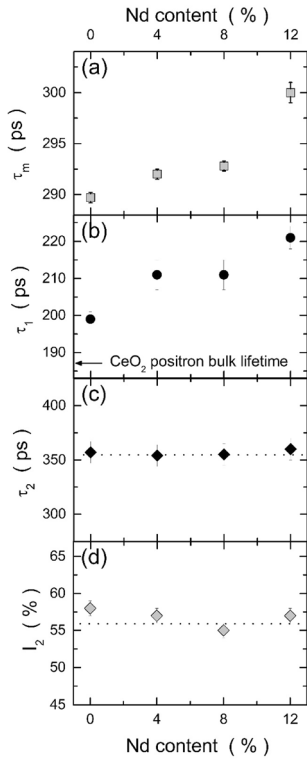


Fig. 3 Evolution of the characteristic parameters of the PALS spectra as a function of the Nd concentration in the cerium dioxide samples: **a** positron mean lifetime τ_m ; **b** first positron lifetime τ_1 ; **c** second positron lifetime τ_2 ; and **d** intensity associated with τ_2

For further analysis, it must be taken into account that:

- (I) all the CeO₂-based nanopowders had particle sizes smaller than 30 nm;
- (II) a typical value of the positron diffusion length in solids was $L_+ \sim 50\text{--}100$ nm.

Therefore, it is reasonable to assume that, under a diffusion-controlled positron trapping regime, most of the positrons injected into a sample become annihilated in open volume defects located in the surface or in the inter-grain regions [56].

Within this framework, and to further analyze the PALS results, the next step was to analyze and discuss the nature and type of positron traps responsible for each positron lifetime component. Note in Fig. 3c and d that not only the values of the second lifetime and its associated intensity were independent of the Nd content in the cerium dioxide samples but they also coincided, within the experimental scatter, with the values obtained for the characteristic parameters of the second lifetime component of pure CeO₂

samples (i.e., $\tau_2 \sim 355$ ps and $I_2 \sim 57\%$, respectively). Owing to its elevated lifetime value, compared with those reported for monovacancies in solids, τ_2 could be assigned to positron annihilation into traps, with typical open volume sizes containing more than a mono- or di-vacancy of an isolated element, i.e., vacancy-like clusters (see discussion below). Besides, such I_2 value indicated the presence of a significant concentration of these large defects in all the samples studied, whose concentration was independent of the Nd content in the Ce_{1-3/4x}Nd_xO₂ samples, at least in the studied composition range.

Recent dynamic force microscopy (DFM) and scanning tunneling microscopy (STM) investigations as well as DFT-based calculations studying the (111) surface of pure CeO₂ have indicated that oxygen vacancies tend to form compact clusters in the surface and/or sub-surface, with different morphologies (e.g., triangular clusters, extended lines, and chains [57, 58]). Furthermore, the results obtained by DFT calculations indicated that these surface and sub-surface oxygen vacancy clusters (OVC) are coordinated exclusively by Ce³⁺ ions [57]. Besides, DFT calculations suggested that OVC also can be formed in RE-doped ceria [59].

On the other hand, different PALS studies aimed to characterize the defect structure in pure CeO₂ and Eu-doped CeO₂ crystallites. In these studies, the authors reported the presence of oxygen vacancy clusters in the surface and/or sub-surface of such Ce-based oxides [17, 60–62]. Based on the experimental and theoretical studies mentioned above, the second positron lifetime component obtained from all the samples analyzed here can be ascribed to positrons trapped and annihilated in OVC defects. Figure 3a and b show that the behavior of the positron mean lifetime and the first lifetime component were in total agreement. This means that the changes in τ were a consequence of the evolution of τ_1 with the Nd content in the Ce_{1-3/4x}Nd_xO₂ samples. Regarding τ_1 , Fig. 3b shows that its value varied from 199 to 221 ps, when increasing the Nd content in the samples. These lifetime values were higher than those reported in the literature for defect-free pure CeO₂, i.e., $\tau_b = 185\text{--}187$ ps [13, 51]. Consequently, the measured values of τ_1 could be interpreted in terms of positron annihilation in open volume defects smaller than the OVC and with a typical size of mono- or di-vacancy. As mentioned above, oxygen vacancy (V_O) is the

predominant defect in pure ceria and in the Re-doped ceria.

Furthermore, as mentioned in the Introduction, the V_O concentration increases with the increase in the Re content. However, it was reported by PALS that V_O is not an effective positron trap, because they are positively charged [63]. For this reason, the shortest lifetime cannot be explained in terms of positron annihilation in isolated oxygen vacancies. In that case, the defect acting as a positron trap should be a complex vacancy-like defect, such as a V_O associate with a negative ion. It is worth mentioning that the effectiveness of this kind of defect in trapping positrons depends on the total charge of the complex vacancy-like defect [64].

In fact, theoretical studies indicated that in pure CeO_2 , a positive V_O forms, together with a Nd^{2+} ion of the nearest neighbor, a neutral $Nd^{2+}-V_O$ associate [65]. In the case of Re-doped ceria systems, it was reported that a Re^{3+} ion substituting a Ce^{4+} ion adjacent to a V_O , forms a neutral $Re^{3+}-V_O$ associate [58, 59]. Due to their neutral charge, this type of associate acts as effective positron traps, characterized by a wide range of positron lifetimes between 236 and 277 ps [60, 61].

It is clear that the τ_1 values presented in Fig. 3b were systematically smaller than those reported for negative ion-vacancy oxygen associates, but they were systematically higher than those obtained for bulk CeO_2 . Consequently, the first lifetime component obtained was the result of a competitive process of positron annihilation in a mixed state as follows: (i) the reduced bulk positron lifetime [18] (in consequence of positron annihilation in OVC); and (ii) the positron annihilation in Nd^{2+} -oxygen-vacancy associates, mainly located at the surface or the sub-surface of the crystallites.

Summarizing, we concluded from PALS results that, as a general trend, an increase of the Nd content in the cerium dioxide samples favored the formation of a higher concentration of small neutral $Nd^{2+}-V_O$ associates. This behavior suggests that oxygen vacancies were formed close to Nd ions, as also reported by A. Sachdeva et al. [66] from PALS studies of a similar Nd-doped CeO_2 system. Furthermore, we also concluded that OVC defects were mainly related to $Re^{(3+)-1}$ ions for Nd-doped or CO exposure. In Fig. 4, a schematic representation of the effect of Nd doping on the defect structure of ceria is shown. In this representation, the addition of Nd favored the

formation of a higher concentration of small neutral $Nd^{2+}-V_O$ associates, rather than bigger oxygen vacancy clusters.

3.3 First-principle results and discussion

Besides the modern experimental techniques, defects as vacancies and substitutional impurities are unavoidable in the growth phase of the material. To address large size, ordering and geometric structure of the nanoparticles, calculations at the atomistic level were performed. To elucidate the key role of oxygen vacancies and the neodymium impurity in the ceria dioxide material, as well as the PALS results and electrical measurements, density functional theory investigations with super-cells were performed. The main results are presented below: Sect. 3.31 describes the calculated structures and spin charge density investigations to understand the cerium and neodymium reductions; in Sect. 3.32 the electronic properties of these geometries are reported; in Sect. 3.33 their thermodynamic stability is discussed, using the formation energy.

3.4 Structural and spin charge density investigations

The pristine ceria dioxide unit cell lattice parameter obtained with DFT calculations is 5.47 Å, whereas in the experimental measurement it has the value of 5.41 Å, with a deviation of only 0.06 Å. Here, we multiplied the CeO_2 unit cell by a factor 2, in the three Cartesian directions, to avoid the interaction between neighboring images. Figure 5 displays the pristine and the defective geometries, both with one (1VacO) and two oxygen vacancies (2VacO_001, 2VacO_002, 2VacO_003), and also with one substitutional neodymium impurity both without (1Nd) and with one oxygen vacancy (1VacO_1Nd). The cerium, oxygen, and neodymium atoms are depicted in blue, red, and yellow, colored spheres. The spin-unpolarized CeO_2 pristine unit cell and supercell contain 12 (4-Ce, 8-O) and 96 (32-Ce, O-64) atoms, respectively; the supercell with one and two oxygen vacancies contain 95 (32-Ce, O-63) and 94 (32-Ce, O-62) atoms, respectively; the one Nd-doped CeO_2 without O-vacancy has 96 (31-Ce, O-64, 1-Nd) atom; the one with O-vacancy contains 95 (31-Ce, O-63, 1-Nd) atoms. One Nd impurity represents the 3.22% of total cerium atoms. The presence of the studied defects in CeO_2 induces

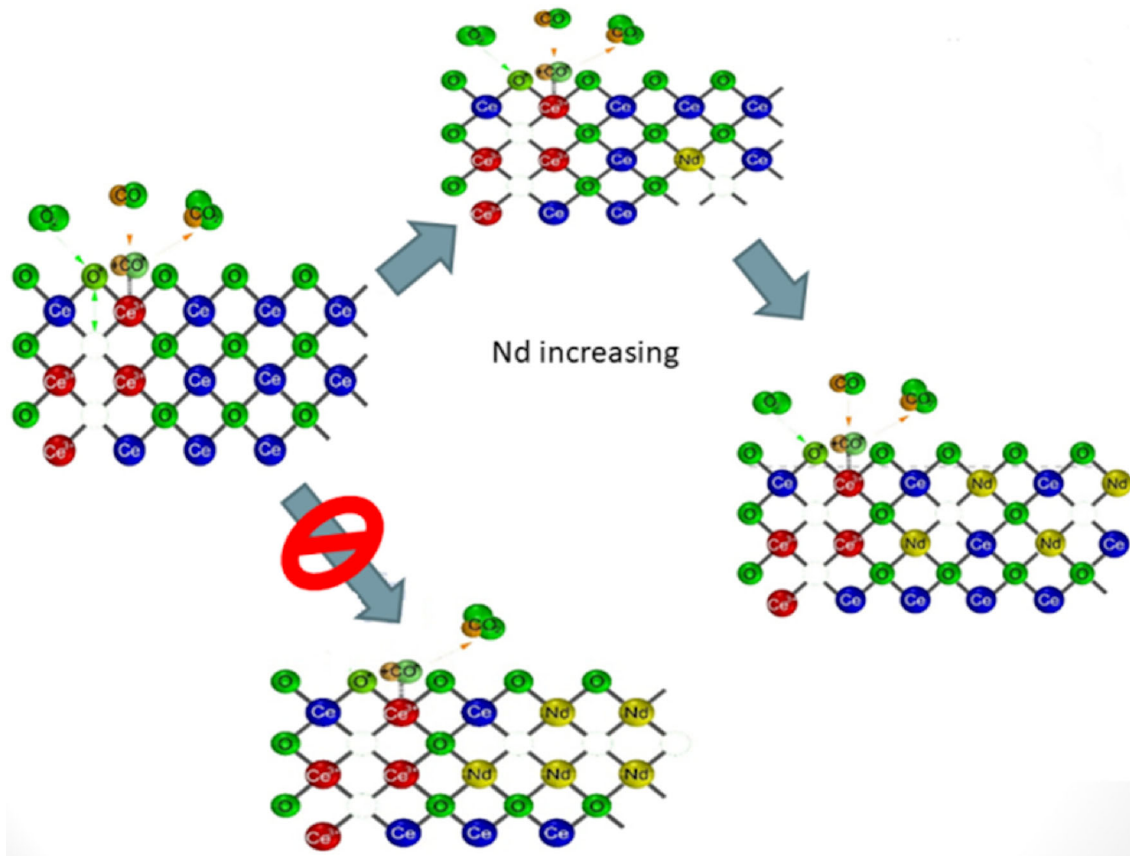


Fig. 4 Graphical scheme of the structural defects induced by Nd addition to ceria

the formation of magnetic moments in the calculated periodic bulk structures. Therefore, the calculated spin charge density (i.e., $\Delta\rho = \rho\uparrow - \rho\downarrow$) is shown, using an isosurface of $+0.01$ (-0.01) $e/\text{\AA}^3$, represented by green (brown) color surrounding the reduced Ce and Nd atoms.

Besides the reduction of the Ce and Nd atoms, the defects change the charge density, the bond lengths, and the chemical environment of the structure. In Fig. 6 the pristine CeO_2 and the defective structures referring to Fig. 5 are shown, where the black arrow indicates the shortening (enlargement) of the chemical bonds of the reduced atoms in 1VacO, 2VacO_001, 2VacO_002, 2VacO_003, 1VacO_1Nd (1Nd) structures and, in consequence, the displacement of the electronic charge density, and the oxygen vacancies are represented by black circles. The shortening of the bond lengths of the atoms surrounding the oxygen vacancies results in a more electropositive charge density in the reduced atoms, while the enlargement of the bond lengths of the substitutional neodymium impurity without the oxygen vacancy gives a more

electronegative charge density in the reduced Nd atom. Moreover, the widening of the atomic bonds of the neodymium atom is due to its larger atomic radius and charge density, compared to the cerium atom ones. However, the reduced Nd in the structure 1VacO_1Nd shows an electropositive charge density. In this way, the oxygen vacancy decreases the electronic density around the neodymium atom. When one oxygen vacancy is near the neodymium impurity in the experimental synthesis, the system is more resistive to the electronic conduction and, according to the experimental observations, the response time for CeO_2 -CO sensor becomes smaller. Therefore, the improved electric conduction is boosted mostly by the reduced Nd^{2+} than the Ce^{3+} , where the oxygen vacancies play a fundamental role.

3.5 Electronic properties: local density of states and magnetic moments

Aiming to understand the crucial role of the defects in the ceria dioxide system, electronic local density of states (LDOS) calculations were performed, both for

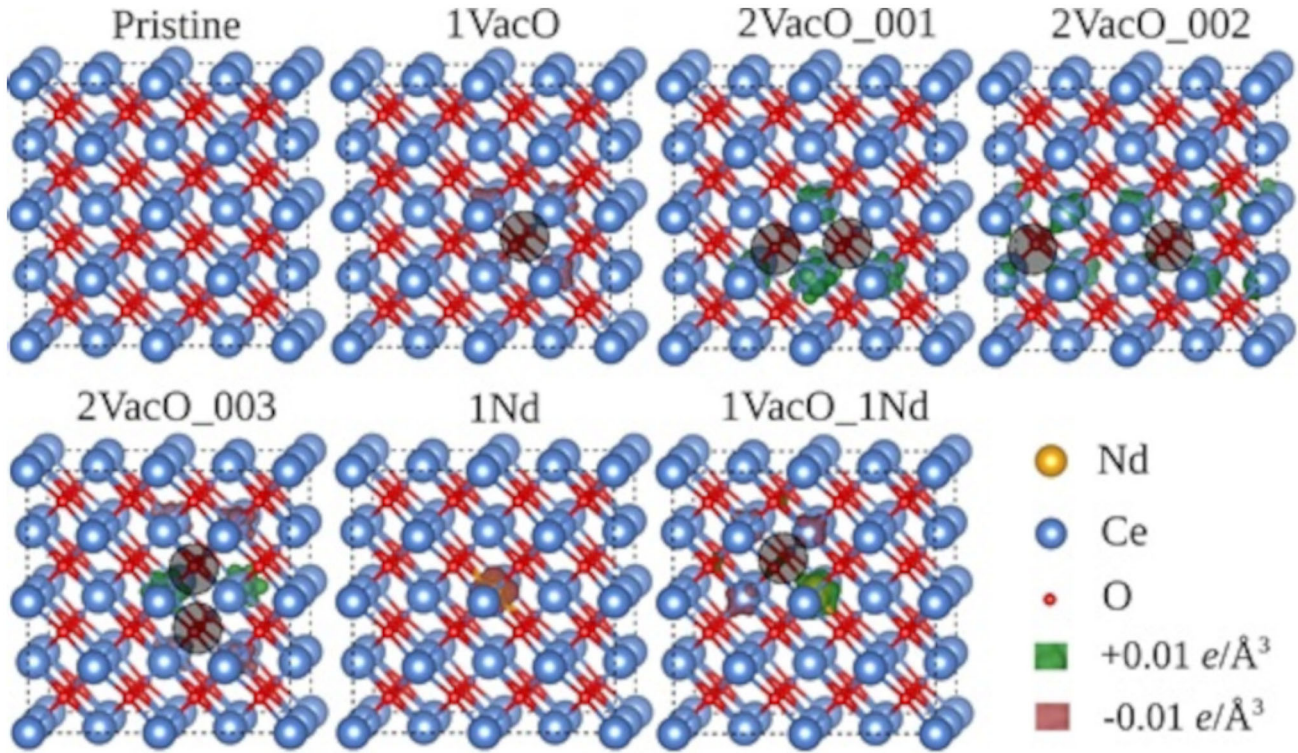
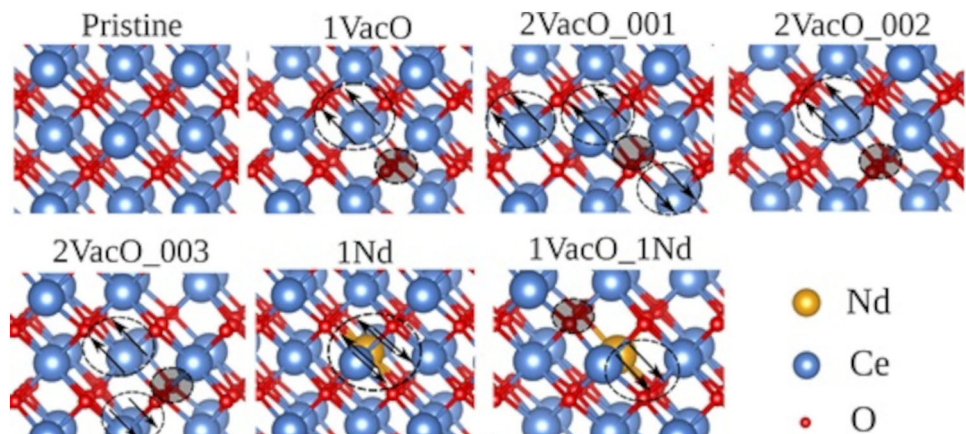


Fig. 5 Ceria dioxide supercell used in present DFT calculation. The CeO_2 without defect (Pristine), as well as the supercell with one oxygen vacancy (1VacO) and two oxygen vacancies in different positions (2VacO_001, 2VacO_002, and 2VacO_003) were investigated. The neodymium replacing one cerium atom without (1Nd) and with oxygen vacancy (1VacO_1Nd) was also

studied. The neodymium, cerium, and oxygen atoms are represented in the yellow, blue, and red colored spheres and the calculated isosurfaces are in green ($+0.01 e/\text{\AA}^3$) and brown ($-0.01 e/\text{\AA}^3$) colors. The oxygen vacancies are identified by black circles (Color figure online)

Fig. 6 CeO_2 bond lengths after DFT calculation. The pristine atomic positions of the ceria dioxide are shown, while the black arrows and circles represents the shortening and enlargement of the reduced atoms. Blue, red, and yellow, colored spheres depict the Ce, O, and Nd atoms (Color figure online)



the pristine CeO_2 and the defective systems, as denoted in Fig. 7. For the pristine geometry, the major contribution in the valence (conduction) band is given by oxygen (cerium) states and, as well known, the 4f-Ce states and p-O states have higher intensity in these atoms.

The optical band gap calculated here, from the valence band (2p-O) to the 4f-Ce states, is 2.83 eV, while the experimental measure is 3.36 eV. This difference is due to the PBE + U functional used in our investigations. Also, the obtained distance between the 4f-Ce states and the conduction band Ce-5d states is 2.78 eV. Thus, these values are within the expected

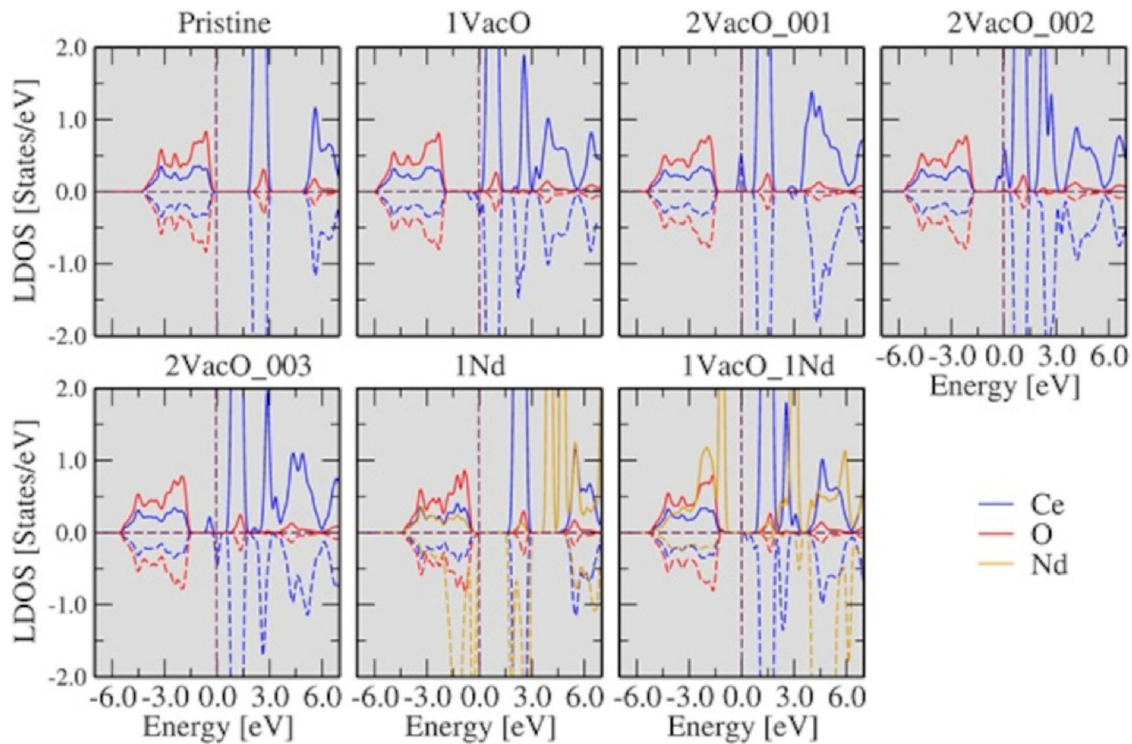


Fig. 7 Local density of states calculations for the structures studied in Fig. 5. The Fermi level was set to zero. The cerium, oxygen, and neodymium states are represented by red, blue, and green colors, respectively (Color figure online)

limits for a good theoretical description of the CeO_2 band structure. It is worth to note that the absence of defects and external perturbations does not provide changes in the oxidation states of the cerium and neodymium atoms. In the 1VacO LDOS investigation, the unoccupied 4f-Ce peak is closer to the Fermi energy in comparison to the LDOS of the pristine geometry. In addition, it was observed for the 1VacO geometry, the presence of the defective 4f-Ce states in the conduction band, and the spin-down states without its counterpart in the valence band, near Fermi energy. The electronic state without its counterpart indicates reduced cerium atoms, from Ce^{4+} to Ce^{3+} , as depicted in Fig. 7. Increasing to two the number of the oxygen vacancies in the CeO_2 supercell, the intensity of the reduced 4f-Ce states increases. The structures 2VacO_001 and 2VacO_002 show the localized spin-up state around the Fermi energy, while the structure 2VacO_003 shows the localized spin-up and down states near Fermi energy. As expected, the total magnetic moment for the one oxygen vacancy structure is of $2.00 \mu\text{B}$, and of $4.00 \mu\text{B}$ for the two oxygen vacancies geometries, where the charge densities are concentrated in the cerium

atoms, due to the presence of the Ce^{3+} in the supercell. It is interesting to note that, the number and position of the oxygen vacancy(ies), is a ruling factor for reduced cerium atoms in the bulk supercell. The 2VacO_002 geometry provides a higher amount of reduced cerium atoms, therefore, with a smaller localized magnetic moment in comparison with the 2VacO_001 and 2VacO_003 structures.

In the 1Nd and 1VacO_1Nd geometries, one neodymium replaces one cerium atom, as also shown in the Fig. 7, where the occupied spin-down and spin-up peaks, respectively, show the Nd reduction. However, the higher magnetic moment in the neodymium atom is given in the 1VacO_1Nd geometry. Basing on these considerations, we can infer that the combination of both defects in the 1VacO_1Nd increase the magnetic moment, boosting the Nd reduction and improving the electronic conduction through 4f-Nd and 4f-Ce states in the doped samples, as discussed in the experimental results section.

3.6 Thermodynamic stability: formation energy

To predict the most preferred geometries in the experimental synthesis and PALS measurements, and to understand the improved electric conduction in the CeO₂ samples due to the reduced Ce³⁺ and Nd²⁺ atoms, the formation energies for the studied structures (shown in Fig. 5) were calculated. The formation energy investigation allows the study of the thermodynamic stability of the oxygen vacancies, the neodymium impurity, and can also guide the experimental techniques toward the desired results. The formation energy (FE) is written as follows (Eq. 2):

$$FE(\alpha) = E_d(\alpha) - E_p(\text{bulk}) - \sum_i = 1\eta_i\mu_i \quad (2)$$

where $E_d(\alpha)$ and $E_p(\text{bulk})$ are the DFT total energies for the defect and pristine geometries indexed by α ; η is the number of atomic species (i) of the system, removed ($\eta < 0$) or added ($\eta > 0$); and μ is the chemical potential of the atoms. The calculation of the formation energy shows the exchange between the chemical potentials of the system and the reservoir. In our system, the chemical potential was obtained with the total energy calculations for spin-polarized Ce and Nd structures in bulk volume, while the O₂ molecule was in gas-phase.

The FE for each calculated structure is represented in Fig. 8 and FE values are reported in Table S.M.1 of the Supplemental Material. Our calculations suggest that the oxygen vacancies have a higher probability to occur in the experimental synthesis than

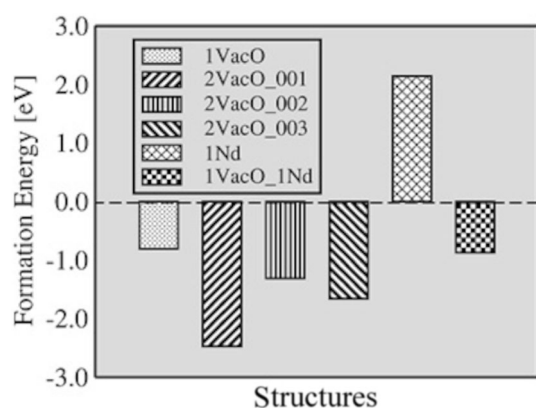


Fig. 8 Formation energies for the calculated structures shown in Fig. 5. Two oxygen vacancies show a higher probability to occur in the experimental synthesis, while the substitutional neodymium impurity increases the formation energy

substitutional neodymium impurity. In addition, two oxygen vacancies have smaller formation energy than the one oxygen vacancy, where the 2VacO_001 is the preferred geometry, thus the most stable thermodynamic structure during the growth phase. Also, a large amount of energy is needed to replace one cerium by one neodymium atom. Therefore, the interstitial cerium and neodymium impurities were not calculated. However, when the neodymium is accompanied by the oxygen vacancy (1VacO_1Nd), the FE decrease, becoming more stable than the structure with only one oxygen vacancy. Thus, the oxygen vacancy plays a key role in the thermodynamic stability of the CeO₂. Among the oxygen vacancies, the thermodynamic stability of the calculated structures is the following: 2VacO_001 > 2VacO_003 > 2VacO_002 > 1VacO. For this reason, by increasing the number of the oxygen vacancies in periodic supercell, also the number of the reduced cerium increases, improving the electronic transport. The structures with closer oxygen vacancies (2VacO_001 and 2VacO_003) show higher thermodynamic stability and greater magnetic moment of the reduced cerium atoms. Also, the position of the oxygen vacancies determines which atoms will be reduced in the CeO₂ material, where the 2VacO_003 geometry has a higher number of reduced cerium atoms in the periodic supercell, however, with a smaller magnetic moment than the other structures with two oxygen vacancies.

It is important to point out that, despite the smaller probability of the structures with the neodymium impurity (1Nd and 1Nd_1VacO), these geometries also occur in the growth phase of the CeO₂, where the most probable structure is the 1Nd_1VacO, according to the experimental observation, where the presence of the Nd impurity induces a single oxygen vacancy in the structure. Thus, given the unavoidable experimental deviation (e.g., the air surrounding the CeO₂ during its growth phase, the temperature effects, and so on), the oxygen vacancies are the predominant defect of the CeO₂ in comparison to the CeO₂ with neodymium substitutional impurity.

3.7 Log (1/Resistance) vs. 1/T curves for calculation of E_a in vacuum atmosphere

In order to obtain the activation energies for different doping concentrations, conductance versus

1/Temperature was evaluated (Fig. 9). An effective activation energy for the electrical conduction process (for films thermally treated in vacuum atmosphere of -104 mmHg) could be estimated from the slope in Fig. 9. These data were obtained after a subsequent cycle of heating up and cooling down in the range of $350\text{--}25$ °C. Then, when there is no change in conductivity as a function of temperature, the slope of the curve during the last heating was obtained. For the cerium-oxide conduction mechanism, the Schottky barrier height (Φ) could not be assumed equal to the activation energy (E_a). In this particular case, the following conditions must be considered:

- (a) due to the size of the clusters, our samples presented overlapped potential barriers. Thus, if we consider the possible presence of a Schottky barrier, then the height (Φ) does not correspond to eVs (band bending). It means that $\Phi \neq \text{eVs} \neq E_a$;
- (b) furthermore, we identified the presence of 4f states in the optical band gap for pure and doped rare-earth samples. These 4f states were near 3.4 eV far from the valence band. Then, electronic conduction was carried out using 4f states of Nd. Therefore, for vacuum and CO atmospheres, we assumed CCCT (cluster-to-cluster charge transfer) [27] conduction instead of electrical conduction through the potential barriers at the grain boundary;
- (c) the whole semiconductor conductance mechanism was thermally favored (thermionic and tunnel conduction) but gas diffusion, and gas

- adsorptions and reactions, in the case of CO, were present. Then, for air and CO exposure, the thermal effect over the electrical transport could not be estimated because of gas-surface interaction, that strongly depends on temperature. The electrical behavior is so affected by the interfaces between grains and, as the surface reaction/adsorption proceeds, the available electrons for conduction at the 4f states change;
- (d) in some cases, we found a p-type semiconductor behavior for CeO_2 samples, also reported in literature [67, 68].

Then, according to our studies, and aiming at measuring an effective E_a for the CCCT proposed for the doped CeO_2 systems [27], only resistance as a function of temperature cycles in a vacuum atmosphere was used. The activation energies are represented in Table 2. A decrease of E_a for CCCT was observed when doping and increasing the Nd percentage from 4 to 12%. This decrease is in agreement with the results obtained in vacuum for R vs. time curve and PALS studies. Moreover, according to G vs. $1/T$ curve, a resistance decrease was observed with an increasing Nd concentration.

In short, from R vs. T studies, we concluded a good correlation with the PALS results. As a general trend, effective activation energies demonstrated that an increase of the Nd content in the cerium dioxide samples favored the electrical conductance, as a consequence of higher concentration of small neutral $\text{Nd}^{2+}\text{-V}_\text{O}$ defective clusters, also confirmed in PALS analysis.

3.8 Resistance vs. time (electrical measurements for vacuum, oxygen, and CO).

The operation temperature must be considered to evaluate the electrical response. From previous reports [28, 69], the electrical resistance as a function of time was measured at 380 °C, as depicted in Fig. 10. The F4 sample (Fig. 10b) presented a better

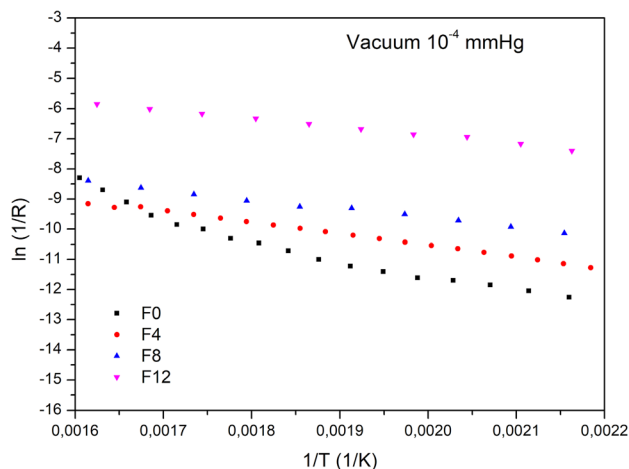


Fig. 9 Arrhenius plots of thick films at different Nd contents: F0; F4; F8; and F12

Table 2 E_a calculated for vacuum atmospheres from an Arrhenius plot

Samples	E_a (± 0.10 eV)
F0	0.58
F4	0.32
F8	0.27
F12	0.24

sensitivity to carbon monoxide than pure ceria (Fig. 10a). Note that the film exposed to reducing atmospheres provokes an increase of electrical currents (electrical resistance decreasing). Oxidant atmospheres, as oxygen exposure, present the opposite effect. As shown in Eqs. 2–4 (Supplementary Material), an increase in the Nd concentration increased the number of vacancies surrounded by electronic densities onto Nd atoms ($4f^1$ states of Nd). The increase of vacancies decreased the available oxygen for CO reaction. Then, when increasing the Nd doping, the CO sensitivity of the samples decreased, as shown in Fig. 10, after CO exposition from 4 to 12%. The response time (t_{resp}) was estimated for each different sample and atmosphere. Pure ceria film exposed to CO presented a t_{resp} of

70 s, while Nd-doped sample presented a t_{resp} of 6 s (see Table 2). As expected, electrical film resistance increased after being exposed to an oxidant atmosphere. This phenomenon was previously associated with the lattice oxygen vacancy annihilation, that reduces the available electron density and disfavors the electrical conduction in samples. Both response and recovery times (Table 3), obtained for the Nd-doped samples, demonstrate that doping with Nd can meaningfully improve ceria-based sensing properties. Furthermore, the comparison results of t_{resp} of Nd and Pr-doped samples [27] show that the Nd doping improves the electrical response time, while changing the atmosphere from vacuum to CO.

Because of the gas adsorption onto the surface, the Fermi level (E_F) and the $4f$ state position changed.

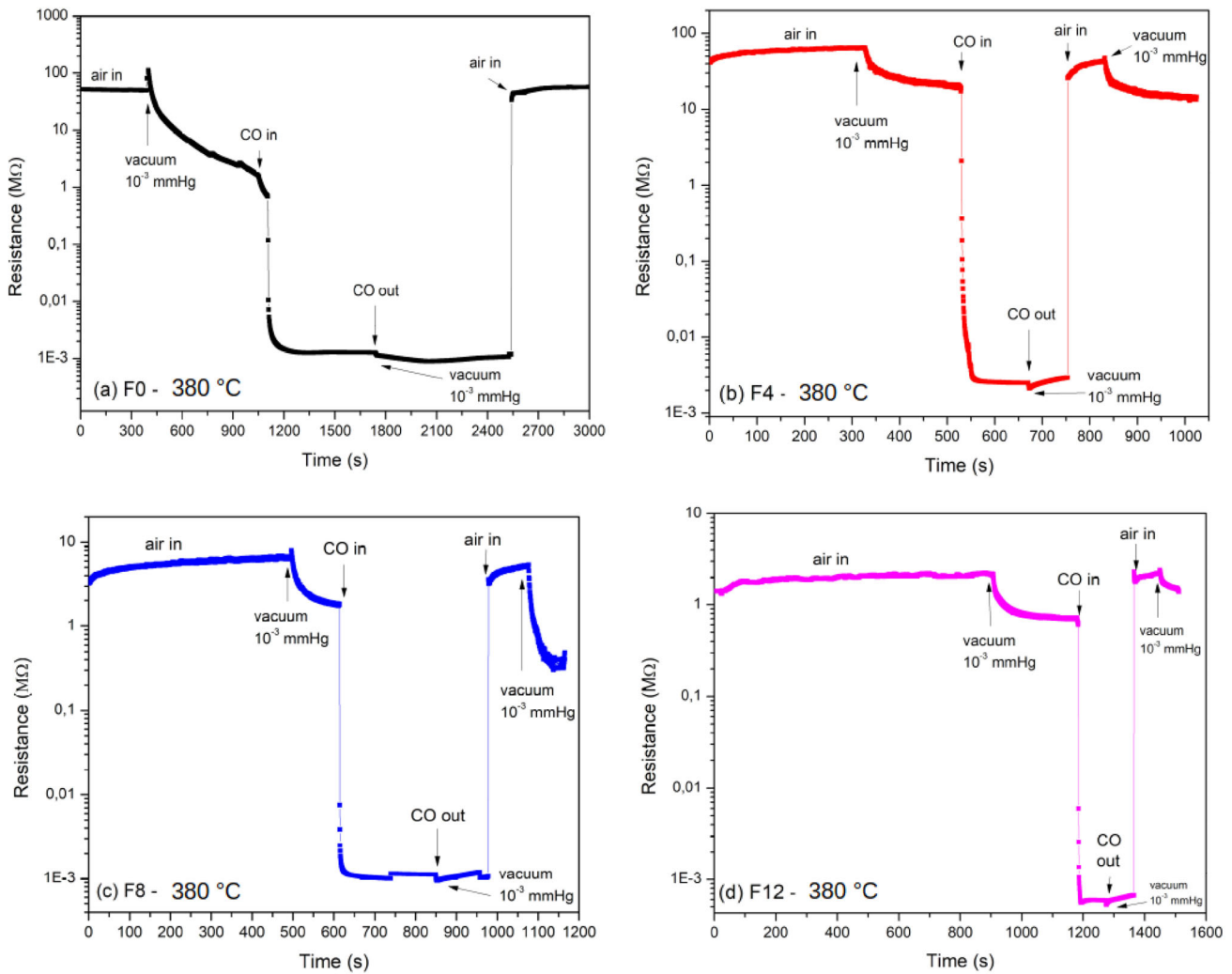


Fig. 10 Electrical Resistance x time of the films **a** F0; **b** F4; **c** F8; and **d** F12

Table 3 Response and recovery times from electrical two-point probe measurements

Samples	Response time (± 0.5 s)	Recovery time (± 0.5 s)
F0	70.0	2.0
F4	11.0	1.0
F8	6.0	1.0
F12	6.0	1.0

The ($E_{4f}-E_F$) difference will be reduced (reductive gases) or increased (oxidant gases) and this E_F level shifting provokes a variation in the number of available conduction electrons (4f state electrons $4f^0 \rightarrow 4f^1$ when Ce^{4+} reduces to Ce^{3+}). Moreover, in the Nd-doped CeO_2 , the electrical conductivity increased because of the E_F movement, as reflected by calculation of E_a in vacuum atmosphere (Table 2).

4 Conclusion

The increase in Nd concentration enhanced the conductivity of the film, given that it favored the CCCT mechanism owing to the creation of structural defects. There was no evidence of an increase in dimers or trimers with the aggregate of Nd using PALS technique. Theoretical results revealed that, when increasing the Nd concentration, the 4f-Nd states were the states that could favorably produce CCCT, with the oxygen vacancies having higher probability to occur in the experimental synthesis than substitutional neodymium impurities. Such mechanism might also be produced by other states involving more energy for network transfer. PALS technique also showed that the adsorption with CO was enhanced with Nd content and the system became more conductive due to the increase in the defects number. Such behavior was ascribed to the increase of the electrical density, which reduced the distance between the clusters, favoring the electronic mobility of the system. The Nd-doped CeO_2 sensor films response to CO gas showed a t_{RESP} of 6 s, owing to the possible Ce^{4+} reduction to Ce^{3+} , affecting the electron number in 4f states and improving its sensing capability. Good response and recovery times, make these materials potential candidates for the manufacturing of commercial gas sensor devices.

Acknowledgments

The authors thank the following agencies for their financial support: FAPEMIG (Brazil) Processes no APQ-03589-16 and APQ-00947-09; FINEP (Brazil) Process no 0745/13; FAPESP (Brazil) Processes no 2018/20590-0, 2018/20729-9, 2016/23891-6, 2017/26105-4 and 2013/07296-2; CNPq (Brazil); CAPES (Brazil); Agencia Nacional de Promoción Científica y Tecnológica (Argentina) Process no PICT 2015-1832; Comisión de Investigaciones Científicas de la Provincia de Buenos Aires (Argentina) and Secretaría de Ciencia, Arte y Tecnología – UNCPBA (Argentina).

Author contributions

All authors contributed equally to the study conception and design of this manuscript.

Data availability

All data generated or analyzed during this study are included in this published article [and its supplementary information files].

Declarations

Conflict of interest The authors have no relevant financial or non-financial interests to disclose.

Supplementary Information: The online version contains supplementary material available at <http://doi.org/10.1007/s10854-022-08098-9>.

References

1. A. Younis, D. Chu, S. Li, *Cerium Oxide Nanostructures and their Applications. Functionalized Nanomaterials* (IntechOpen, London, 2016)
2. Q. He, Experimental study on polishing performance of CeO_2 and nano - SiO_2 mixed abrasive. *Appl. Nanosci.* **8**, 163–171 (2018)
3. D. Majumder, S. Roy, Development of low-ppm CO sensors using pristine CeO_2 nanospheres with high surface area. *ACS Omega* **3**, 4433–4440 (2018)

4. S. Rajeshkumar, P. Naik, Synthesis and biomedical applications of Cerium oxide nanoparticles: a review. *Biotechnol. Rep.* **17**, 1–5 (2018)
5. R. Meng et al., Cerium-oxide-modified anodes for efficient and UV-stable ZnO-based perovskite solar cells. *ACS Appl. Mater. Interfaces* **11**, 13273–13278 (2019)
6. M. Farahmandjou, M. Zarinkamar, T.P. Firoozabadi, Synthesis of cerium oxide (CeO₂) nanoparticles using simple CO-precipitation method. *Rev. Mex. Fis. Mex. Fis.* **62**, 496–499 (2016)
7. A. Valentini et al., Ni:CeO₂ nanocomposite catalysts prepared by polymeric precursor method. *Appl. Catal. A Gen.* **310**, 174–182 (2006)
8. A.I.Y. Tok, F.Y.C. Boey, Z. Dong, X.L. Sun, Hydrothermal synthesis of CeO₂ nano-particles. *J. Mater. Process. Technol.* **190**, 217–222 (2007)
9. K. Ocakoglu et al., Microwave-assisted hydrothermal synthesis and characterization of ZnO nanorods. *Spectrochim. Acta Part A* **148**, 362–368 (2015)
10. R. Schmidt, J.P. Gonjal, E. Morán, Microwaves: microwave assisted hydrothermal synthesis of nanoparticles, in *Concise Encyclopedia of Nanotechnology*. ed. by B.I. Kharisov, O.V. Kharissova, U. Ortiz-Mendez (CRC Press Taylor & Francis Group, Boca Raton, 2015), pp. 561–572
11. L.-Y. Meng, B. Wang, M.-G. Ma, K.-L. Lin, The progress of microwave-assisted hydrothermal method in the synthesis of functional nanomaterials. *Mater. Today Chem.* **1–2**, 63–83 (2016)
12. R.C. Deus et al., Influence of mineralizer agents on the growth of crystalline CeO₂ nanospheres by the microwave-hydrothermal method. *J. Alloys Compd.* **550**, 245–251 (2013)
13. R.C. Deus et al., Electrical behavior of cerium dioxide films exposed to different gases atmospheres. *Ceram. Int.* **42**, 15023–15029 (2016)
14. Y.J. Acosta-Silva et al., Nanostructured CeO₂ thin films prepared by the sol-gel dip-coating method with anomalous behavior of crystallite size and bandgap. *J. Nanomater.* **2019**, 1–8 (2019)
15. A. Bandyopadhyay, B.J. Sarkar, S. Sutradhar, J. Mandal, P.K. Chakrabarti, Synthesis, structural characterization, and studies of magnetic and dielectric properties of Gd³⁺ doped cerium oxide (Ce_{0.90}Gd_{0.10}O_{2-δ}). *J. Alloys Compds.* **865**, 158838 (2021)
16. M. Batzill, U. Diebold, The surface and materials science of tin oxide. *Prog. Surf. Sci.* **79**, 47–154 (2005)
17. K. Sudarshan, V. Tiwari, P. Utpalla, S.K. Gupta, Defect evolution in Eu³⁺, Nb⁵⁺ doped and co-doped CeO₂: X-ray diffraction, positron annihilation lifetime and photoluminescence studies. *Inorg. Chem. Front.* **6**, 2167–2177 (2019)
18. P. Hautojärvi, C. Corbel, Positron spectroscopy of defects in metals and semiconductors, in *Positron Spectroscopy of Solids*. ed. by P. Hautojärvi, C. Corbel (IOS Press, Amsterdam, 1995), pp. 491–532
19. P.R.L. Keating, D.O. Scanlon, B.J. Morgan, N.M. Galea, G.W. Watson, Analysis of intrinsic defects in CeO₂ using a koopmans-like GGA+U approach. *J. Phys. Chem. C* **116**, 2443–2452 (2012)
20. M. Schüler, N. Helwig, A. Schütze, T. Sauerwald, G. Ventura, Detecting trace-level concentrations of volatile organic compounds with metal oxide gas sensors. *Sensors2013 IEEE*, 1–4 (2013). <https://doi.org/10.1109/ICSENS.2013.6688276>
21. S. Samadi, G. Asadi Cordshooli, M. Yousefi, K. Kalateh, S.A. Zakaria, CeO₂/TiO₂ core/shell nanoparticles as quantitative gas sensor at room temperature. *Sens. Rev.* **38**, 458–466 (2018)
22. K. Yuan et al., Fabrication of a micro-electromechanical system-based acetone gas sensor using CeO₂ nanodot-decorated WO₃ nanowires. *ACS Appl. Mater. Interfaces* **12**, 14095–14104 (2020)
23. J. Hu et al., Highly sensitive and ultra-fast gas sensor based on CeO₂-loaded In₂O₃ hollow spheres for ppb-level hydrogen detection. *Sens. Actuators B Chem.* **257**, 124–135 (2018)
24. D.E. Motaung et al., Ultra-high sensitive and selective H₂ gas sensor manifested by interface of n–n heterostructure of CeO₂-SnO₂ nanoparticles. *Sens. Actuators B Chem.* **254**, 984–995 (2018)
25. C. Mattiuzzi, G. Lippi, Worldwide epidemiology of carbon monoxide poisoning. *Hum. Exp. Toxicol.* **39**, 387–392 (2020)
26. H.-T. Chen, First-principles study of CO adsorption and oxidation on Ru-doped CeO₂(111) surface. *J. Phys. Chem. C* **116**, 6239–6246 (2012)
27. R. Cristina de Oliveira et al., Charge transfer in Pr-doped cerium oxide: experimental and theoretical investigations. *Mater. Chem. Phys.* **249**, 122967 (2020)
28. L.S.R. Rocha et al., Novel gas sensor with dual response under CO(g) exposure: optical and electrical stimuli. *Phys. B Condens. Matter* **536**, 280–288 (2018)
29. L.S.R. Rocha et al., Experimental and ab initio studies of deep-bulk traps in doped rare-earth oxide thick films. *J. Phys. Chem. C* **124**, 997–1007 (2020)
30. R.C. de Oliveira et al., Influence of synthesis time on the morphology and properties of CeO₂ nanoparticles: an experimental-theoretical study. *Cryst. Growth Des.* **20**, 5031–5042 (2020)
31. A.C. Larson, R.B. Von Dreele, *General Structure Analysis System (GSAS)*. **748** (2004)
32. B.H. Toby et al., EXPGUI, a graphical user interface for GSAS. *J. Appl. Crystallogr.* **34**, 210–213 (2001)

33. B.D. Viezbicke, S. Patel, B.E. Davis, D.P. Birnie III., Evaluation of the Tauc method for optical absorption edge determination: ZnO thin films as a model system. *Phys. status solidi* **252**, 1700–1710 (2015)
34. D. Giebel, J. Kansy, A new version of LT program for positron lifetime spectra analysis. *Mater. Sci. Forum* **666**, 138–141 (2010)
35. N. Tibaldi et al., Un dispositivo de caracterización optoelectrónica de materiales (2015)
36. N. Tibaldi et al., Dispositivo de caracterização optoeletrônica de materiais (2016)
37. Z. Lu, Z. Yang, Interfacial properties of NM/CeO₂(111) (NM = noble metal atoms or clusters of Pd, Pt and Rh): a first principles study. *J. Phys. Condens. Matter* **22**, 475003 (2010)
38. S. Shi et al., O-vacancy and surface on CeO₂: a first-principles study. *J. Phys. Chem. Solids* **71**, 788–796 (2010)
39. C.-Y. Zhou, D. Wang, X.-Q. Gong, A DFT+U revisit of reconstructed CeO₂(100) surfaces: structures, thermostabilities and reactivities. *Phys. Chem. Chem. Phys.* **21**, 19987–19994 (2019)
40. J.P. Perdew, K. Burke, M. Ernzerhof, Generalized gradient approximation made simple. *Phys. Rev. Lett.* **77**, 3865–3868 (1996)
41. N.V. Skorodumova, M. Baudin, K. Hermansson, Surface properties of CeO₂ from first principles. *Phys. Rev. B* **69**, 75401 (2004)
42. X. Gonze, F. Finocchi, Pseudopotentials plane waves? Projector augmented waves: a primer. *Phys. Scr.* **T109**, 40 (2004)
43. N.A.W. Holzwarth, G.E. Matthews, R.B. Dunning, A.R. Tackett, Y. Zeng, Comparison of the projector augmented-wave, pseudopotential, and linearized augmented-plane-wave formalisms for density-functional calculations of solids. *Phys. Rev.* **55**, 2005 (2005)
44. J. Hafner, G. Kresse, The Vienna AB-initio simulation program VASP: an efficient and versatile tool for studying the structural, dynamic, and electronic properties of materials BT - properties of complex inorganic solids, in *Properties of Complex Inorganic Solids*. ed. by A. Gonis, A. Meike, P.E.A. Turchi (Springer, Boston, 1997), pp. 69–82
45. J. Hafner, Ab-initio simulations of materials using VASP: density-functional theory and beyond. *J. Comput. Chem.* **29**, 2044–2078 (2008)
46. G. Sun et al., Performance of the Vienna ab initio simulation package (VASP) in chemical applications. *J. Mol. Struct. THEOCHEM* **624**, 37–45 (2003)
47. S.L. Dudarev, G.A. Botton, S.Y. Savrasov, C.J. Humphreys, A.P. Sutton, Electron-energy-loss spectra and the structural stability of nickel oxide: an LSDA+U study. *Phys. Rev. B* **57**, 1505–1509 (1998)
48. S.J. Hong, A.V. Virkar, Lattice parameters and densities of rare-earth oxide doped ceria electrolytes. *J. Am. Ceram. Soc.* **78**, 433–439 (1995)
49. J.P. Nair, E. Wachtel, I. Lubomirsky, J. Fleig, J. Maier, Anomalous expansion of CeO₂ nanocrystalline membranes. *Adv. Mater.* **15**, 2077–2081 (2003)
50. A. Trovarelli, Structural and oxygen storage/release properties of CeO₂-based solid solutions. *Comments Inorg. Chem.* **20**, 263–284 (1999)
51. I. Nurhasanah, M. Abdullah, Khairurrijal, Structure and morphology of neodymium-doped cerium oxide solid solution prepared by a combined simple polymer heating and D.C.-Magnetron sputtering method. *AIP Conf. Proc.* **989**, 147–150 (2008)
52. S.K. Abdel-Aal, A.S. Abdel-Rahman, Graphene influence on the structure, magnetic, and optical properties of rare-earth perovskite. *J. Nanoparticle Res.* **22**, 267 (2020)
53. S.K. Abdel-Aal, A.I. Beskrovnyi, A.M. Ionov, R.N. Mozhchil, A.S. Abdel-Rahman, Structure investigation by neutron diffraction and X-ray diffraction of graphene nanocomposite CuO-rGO prepared by low-cost method. *Phys. Status Solidi* **218**, 2100138 (2021)
54. J. Cizek et al., Defect studies of nanocrystalline zirconia powders and sintered ceramics. *Phys. Rev. B* **81**, 024116 (2010)
55. C. Macchi, M.A. Ponce, P.M. Desimone, C.M. Aldao, A. Somoza, Vacancy-like defects in nanocrystalline SnO₂: influence of the annealing treatment under different atmospheres. *Philos. Mag.* **98**, 673–692 (2018)
56. H.-E. Schaefer, R. Würschum, R. Birringer, H. Gleiter, Structure of nanometer-sized polycrystalline iron investigated by positron lifetime spectroscopy. *Phys. Rev. B* **38**, 9545–9554 (1988)
57. F. Esch et al., Electron localization determines defect formation on ceria substrates. *Science (80-)* **309**, 752–755 (2005)
58. Z.-K. Han, Y.-Z. Yang, B. Zhu, M.V. Ganduglia-Pirovano, Y. Gao, Unraveling the oxygen vacancy structures at the reduced CeO₂ (111) surface. *Phys. Rev. Mater.* **2**, 35802 (2018)
59. M. Coduri, S. Checchia, M. Longhi, D. Ceresoli, Rare earth doped ceria: the complex connection between structure and properties. *Front. Chem.* **6**, 1–23 (2018)
60. A.V. Thorat, T. Ghoshal, J.D. Holmes, P.M.G. Nambissan, M.A. Morris, A positron annihilation spectroscopic investigation of europium-doped cerium oxide nanoparticles. *Nanoscale* **6**, 608–615 (2014)
61. L. Wang et al., Oxygen vacancy clusters essential for the catalytic activity of CeO₂ nanocubes for o-xylene oxidation. *Sci. Rep.* **7**, 1–11 (2017)

62. L. Xiangwen, Z. Kebin, W. Lei, W. Baoyi, L. Yadong, Oxygen vacancy clusters promoting reducibility and activity of ceria nanorods. *J. Am. Chem. Soc.* **131**, 3140–3141 (2009)
63. R. Krause-Rehberg, H.S. Leipner, *Positron Annihilation Semiconductors* (Springer, Berlin, 1999)
64. K. Saarinen, P. Hautojärvi, C. Corbel, Chapter5 Positron annihilation spectroscopy of defects in semiconductors, in *Identification of Defects in Semiconductors*. ed. by M.B.T.S. Stavola (Elsevier, Amsterdam, 1998), pp. 209–285
65. N.V. Skorodumova, S.I. Simak, B.I. Lundqvist, I.A. Abrikosov, B. Johansson, Quantum origin of the oxygen storage capability of ceria. *Phys. Rev. Lett.* **89**, 166601 (2002)
66. A. Sachdeva, S.V. Chavan, A. Goswami, A.K. Tyagi, P.K. Pujari, Positron annihilation spectroscopic studies on Nd-doped ceria. *J. Solid State Chem.* **178**, 2062–2066 (2005)
67. B. Wang et al., Fast ionic conduction in semiconductor CeO₂- δ electrolyte fuel cells. *NPG Asia Mater.* **11**, 51 (2019)
68. H. Yokokawa et al., Thermodynamic reconsiderations on electronic properties of pure- and doped-ceria. *ECS Trans.* **28**, 165 (2010)
69. P.P. Ortega et al., Towards carbon monoxide sensors based on europium doped cerium dioxide. *Appl. Surf. Sci.* **464**, 692–699 (2019)

Publisher's Note Springer Nature remains neutral with regard to jurisdictional claims in published maps and institutional affiliations.